

# Amine-Mediated Cosolvent Polymerization for Tunable Mesoporous-Microporous Double-Shell Carbon Spheres toward High-Performance Supercapacitors

Zhi-Yan Bai, Zha-Xi Wan-Me, Ji Cai-Rang, Peng Liu, Fu Yang, and Yu-Long Xie\*

Porous carbon materials attract great interest due to their wide range of applications in electrochemical energy systems, especially in structured and pore size-tunable carbon materials prepared by template-assisted methods. In this study, a solvent-mediated polymerization-induced self-assembly strategy is designed for the synthesis of hierarchical double-shell-layer porous carbon nanospheres, and screened out the carbon nanospheres N-doped hierarchical meso-microporous carbon spheres (NPCS)-40 with the best morphology and performance by

exploring the effects of different 1,3,5-trimethylbenzene contents, different cosolvent ratios, different cosurfactant ratios, as well as different ethylenediamine and resorcinol contents on the carbon nanospheres' structure. The resulting carbon nanospheres exhibit a specific capacitance of  $249 \text{ F g}^{-1}$  in a supercapacitor with a current density of  $0.5 \text{ A g}^{-1}$  and  $139.4 \text{ F g}^{-1}$  in a symmetric supercapacitor with excellent stability, which is maintained at 117% after 5000 charging and discharging cycles.

## 1. Introduction

In recent years, domestic coal has been in short supply, a large amount of industrial waste gas, automobile exhaust emissions pollution is becoming increasingly serious, as well as the imminent depletion of coal resources, biomass, tidal energy, geothermal energy, solar energy, and other reusable clean energy development and reserves have become a hot issue. To solve the instability and intermittency of these energy storage systems, it is necessary to find an energy storage and conversion system with good cycle stability and high efficiency.<sup>[1–4]</sup> The energy storage mechanism of supercapacitors (SCs) originates from the rapid charge storage and release process at or near the surface of the electrode material. Unlike batteries that rely on bulk-phase ion embedding/de-embedding reactions, their charge storage relies on two main modes: bilayer capacitance and pseudocapacitance. Bilayer capacitors achieve charge separation through electrostatic adsorption between the electrode surface and electrolyte ions, a highly reversible physical process that gives the device ultra-long cycling stability; pseudo-capacitors store charge through a rapid redox reaction (e.g., the Faraday process for metal oxides) at the active sites on the electrode surface, which significantly improves energy density.<sup>[5]</sup> However, the synergistic effect

of the two is limited by the design of the material structure and the optimization of the interface dynamics.<sup>[6–8]</sup> For example, although the micropores of carbon-based materials can provide a high specific surface area, the small pore size will hinder ion transport, resulting in low effective utilization; pseudocapacitive materials (e.g.,  $\text{MnO}_2$ , conductive polymers) can contribute extra capacity, but the balance between the reaction depth and the structural stability of the materials is still a technical difficulty. For this reason, researchers in recent years have proposed two major strategies, namely "hierarchical porous structure" and "composite electrode system": the former is designed through the synergistic design of microporous ( $<2 \text{ nm}$ ), mesoporous ( $2\text{--}50 \text{ nm}$ ), and macroporous ( $>50 \text{ nm}$ ), which ensures a high surface area while optimizing the ion diffusion path; the latter is designed to optimize the ion diffusion path; and the latter is designed to optimize the ion diffusion path. The latter, through the composite of carbon-based materials and pseudo-capacitive active substances (e.g. graphene-loaded  $\text{RuO}_2$  nanoparticles), achieves the synergistic efficiency of the bilayer and Faraday storage, and increases the energy density to  $30\text{--}50 \text{ Wh kg}^{-1}$ , which is close to the level of lead-acid batteries.<sup>[9–12]</sup> Despite significant progress in materials innovation, the actual performance of SCs is still constrained by multiple factors. First, the efficiency of the electron/ion conduction network of the electrode material directly affects the power density. For example, although graphene has ultra-high conductivity, its lamellar stacking will block the ion channels, and needs to be designed through a 3D porous structure (such as foam graphene) or composite with carbon nanotubes to build a continuous conductive network.<sup>[11,13,14]</sup> Second, the chemical stability and voltage window of the electrolyte determine the upper energy limit of the device. Traditional aqueous electrolytes (e.g.,  $\text{H}_2\text{SO}_4$ ) are limited by a decomposition voltage of 1.2 V, while ionic liquid electrolytes can extend the

Z.-Y. Bai, Z.-X. Wan-Me, J. Cai-Rang, P. Liu, F. Yang, Y.-L. Xie  
 School of Chemistry and Materials Science  
 Key Laboratory of Resource Chemistry and Eco-environmental Protection  
 in Tibetan Plateau of State Ethnic Affairs Commission  
 Qinghai Provincial Key Laboratory of Nanomaterials and Nanotechnology  
 Qinghai Minzu University  
 Xining 810007, China  
 E-mail: yulongxie2012@126.com

 Supporting information for this article is available on the WWW under <https://doi.org/10.1002/batt.202500418>

voltage window to 3–4 V. However, ion migration resistance due to high viscosity requires a breakthrough in new low-impedance electrolytes (e.g., quasisolid gels). In addition, interfacial side reactions (e.g., oxidation of carbon materials, dissolution of metal oxides) during long-term cycling can trigger capacity degradation, which needs to be suppressed by surface cladding (e.g., ALD-deposited  $\text{Al}_2\text{O}_3$  protective layer) or solid-state electrolyte encapsulation.<sup>[15]</sup> The solution to these challenges relies on cross-scale research—from atomic-level surface modification to macroscopic device integration, and systematic innovation from fundamental electrochemical mechanisms to engineered preparation processes.<sup>[12,16]</sup>

Among many energy materials, carbon materials have received great attention from researchers due to their high specific surface area and excellent electrochemical ability; thus, there is a strong interest in the application of SCs.<sup>[17–20]</sup> Mesoporous carbon materials, due to their high specific surface area, adjustable pore size distribution, excellent chemical stability and electrical conductivity, have shown great potential for application in the fields of energy storage (e.g., SCs, lithium-ion batteries), catalysis (e.g., catalyst carriers, electrocatalysis<sup>[21]</sup>), environmental treatment (e.g.,  $\text{CO}_2$  capture, organic pollutant adsorption), and biomedical (e.g., drug delivery, biosensing). However, the traditional synthesis methods of mesoporous carbon materials (e.g., hard template method, soft template method) still have significant challenges in terms of precise regulation of pore size, structural order, and functional design.<sup>[22–26]</sup> For example, it is difficult to achieve the synergistic construction of multilevel pores by a single template method, while the complexity of solvent volatilization kinetics and crosslinking reactions often leads to uneven material morphology or pore collapse. Therefore, exploring novel synthesis strategies to break through the structure and performance bottleneck of mesoporous carbon materials has become a current research hotspot in the field of materials science.<sup>[11,27–31]</sup>

In this context, the dual-surfactant cointemplating method has gradually gained attention due to its unique micelle assembly behavior and tunability. Through the rational choice of surfactant combinations (e.g., triblock copolymer P123 and F127), diverse designs of mesoporous structures (e.g., bimodal pore sizes, graded pores) can be achieved, and the mass transfer efficiency and mechanical strength of the materials can be optimized.<sup>[32–34]</sup> However, most of the existing studies focus on single surfactant systems, and there is still a lack of systematic knowledge on the mechanism of dual surfactant ratio regulation and its effect on the properties of carbon materials. In addition, the correlation between key parameters such as solvent composition (e.g., ethanol/water ratio) and crosslinking agent (e.g., ethylenediamine) concentration and the synergistic effect of surfactants has not yet been clarified, which limits the further promotion of this method.<sup>[35–37]</sup>

The dual-surfactant synergistic templating method can achieve precise regulation of micelle size and morphology by regulating the hydrophilic–hydrophobic balance of different surfactants. For example, the complex system of P123 ( $\text{EO}_{20}\text{PO}_{70}\text{EO}_{20}$ ) and F127 ( $\text{EO}_{106}\text{PO}_{70}\text{EO}_{106}$ ) can form mixed micelles due to the difference in the length of their PPO chain segments, which

can be oriented to mesoporous structures with different pore sizes.<sup>[38–41]</sup> Kim et al. found that when the ratio of P123/F127 is 7:3, the size distribution of the mixed micelles is the narrowest, and the corresponding pore sizes of mesoporous carbon materials are concentrated at 8–10 nm, and the pores are hexagonal. Concentrated at 8–10 nm, and the pores were arranged in hexagonal order. However, most of the existing studies focus on the static behavior of micelles and lack in-depth analysis of the competition mechanism of bis-surfactants in the dynamic synthesis process (e.g., solvent evaporation, precursor crosslinking).<sup>[1,42–44]</sup>

Ethylenediamine (EDA), as a crosslinking agent and nitrogen source, can form a 3D crosslinking network and enhance the stability of the carbon skeleton through the condensation reaction between the amino group and the hydroxyl group during the polymerization of phenolic resins or polydopamine. Meanwhile, the pyrolysis products of EDA can effectively dope nitrogen atoms to enhance the surface polarity and electrochemical activity of the materials. It is shown that the concentration of EDA significantly affects the crosslinking degree and pore structure: when the amount of EDA is 10 wt%, the nitrogen content of mesoporous carbon can reach 5.2 at%, and the proportion of pyridine nitrogen is more than 60%.<sup>[45,46]</sup> However, excessive EDA can lead to an increase in system pH, destabilizing surfactant micelles and triggering mesopore collapse or morphological distortion. How to balance the crosslinking effect of EDA with the template-directed effect is still a technical difficulty in this field.

In this study, we focus on the “amine-mediated polymerization-induced synthesis”, combining the microemulsion method with the dual surfactant (P123/F127) synergistic templating strategy, and systematically investigate the effects of ethylenediamine crosslinking behavior, solvent polarity regulation and surfactant ratio on the structure (pore size distribution, morphological homogeneity, nitrogen doping level) and properties (specific surface area, electrochemical activity, adsorption capacity) of mesoporous carbon materials. (specific surface area, electrochemical activity, adsorption capacity) of mesoporous carbon materials. The results will not only provide theoretical guidance for the controlled synthesis of hierarchical porous carbon materials but also promote their practical applications in energy and environmental fields.

Compared to conventional template-assisted methods (e.g., hard/soft templating), our amine-mediated cosolvent polymerization-induced self-assembly strategy offers three distinct advantages: (1) the dual-surfactant (P123/F127) system enables precise control over micelle size and morphology, facilitating the formation of hierarchical microporous-mesoporous double-shell structures in a single step, which is challenging to achieve with single-template methods.<sup>[20,22–25]</sup> (2) The solvent-mediated approach (ethanol/water system) dynamically regulates micelle stability and precursor crosslinking, avoiding pore collapse during solvent evaporation common issue in static templating.<sup>[1,4]</sup> (3) Ethylenediamine (EDA) acts as both a crosslinker and nitrogen dopant, eliminating the need for post-synthesis modification while enhancing electrochemical activity.<sup>[45,46]</sup> This synergistic approach outperforms recent reports on hollow carbon spheres (e.g., microemulsion-derived mesoporous carbons or  $\text{SiO}_2$ -templated

materials) in terms of structural tunability, nitrogen doping efficiency, and scalability.

## 2. Results and Discussion

Figure 1a shows the scanning electron microscopy image of porous carbon nanospheres induced by emulsion polymerization self-assemble, with an average diameter of about 350 nm. After removing the copolymer micelle template, uniform and monodisperse polyphenol carbon nanospheres were formed on the main structure of phloroglucinol-ethylenediamine. According to Figure 1b,c, all mesopores of the mesoporous carbon spheres are open, and according to the high-magnification scanning electron microscopy Figure 1d, the mesopores are uniformly distributed on the surface of the nanospheres. Carbonized at 800 °C under N<sub>2</sub> atmosphere, the obtained nitrogen-containing mesoporous carbon nanospheres still maintain a monodisperse spherical morphology without deformation. The presence of several angles of mesoporous carbon nanospheres in Figure 1b,c shows that there are hollows with a diameter of about 50–150 nm on the top. According to the analysis in Figure 1c, the nanospheres are suspected to have a hollow structure, which was confirmed by transmission electron microscopy. High-angle annular dark-field imaging-energy dispersive X-ray spectroscopy (HAADF-EDX) (Figure 1e) confirms uniform spherical morphology with porous surfaces. Elemental mapping shows a homogeneous distribution of C, N, and O.

Transmission electron microscopy confirms the nanosphere structure, as shown in Figure 2a,b, which is a hollow structure with cavities on the sphere, as shown in Figure 2b. TEM (Figure 2d) reveals a double-shell structure with outer mesopores ( $\approx 8$  nm) and inner micropores. BET analysis (Table 2) quantifies the meso/microporous volume ratio as 1.85:1, as shown in Figure 2d, which can more intuitively and clearly show that the

mesoporous carbon nanosphere has a microporous-mesoporous double-shell structure, with the outer layer being a mesoporous structure and the inner layer being a microporous structure. Figure 2e can be observed that the diameter of the mesoporous channels on the outer layer of the carbon nanosphere is about 8 nm. This microporous-to-mesoporous gradient pore structure provides a hierarchical diffusion path for electrolyte ion transport.<sup>[43]</sup>

Figure 2c,f show the N<sub>2</sub> adsorption-desorption isotherms and pore size distribution of mesoporous carbon material NPCS-40. The pore size distribution completely conforms to the results analyzed by TEM. This material has micropores and mesopores, with mesopore diameters of about 8 nm. In the N<sub>2</sub> atmosphere carbonization process of mesoporous carbon nanoparticles, low-temperature carbonization forms a microporous carbon core. In the later high-temperature carbonization process, the outer layer of polymer micelles forms a mesoporous template. After high-temperature carbonization, the template is removed to generate a mesoporous shell layer. The inner micropores provide a high specific surface area, and the mesoporous shell promotes mass transfer kinetics, avoiding micropore blockage.

Figure 2g shows that NPCS-40 has a hexagonal mesoporous structure. The high electrical conductivity and open pore channels of hexagonal mesoporous carbon can enhance the rate of ion transport. Figure 2i is the selected area diffraction pattern of the sample in Figure 2h. From the figure, diffraction rings of the (002) and (101) crystal planes can be observed. Selected area electron diffraction shows that the sample exhibits polycrystalline diffraction characteristics, with two continuous concentric diffraction rings observed (Figure 2i). The calculated interplanar spacings corresponding to each ring are  $d_1 = 3.04$  and  $d_2 = 2.01$  Å, matching the (002) and (101) crystal planes of graphite. The typical interlayer spacing of graphite,  $d_{002} \approx 3.35$  Å, indicates that the material has interlayer compression or structural deviation from ideal graphite. The perfect match between the

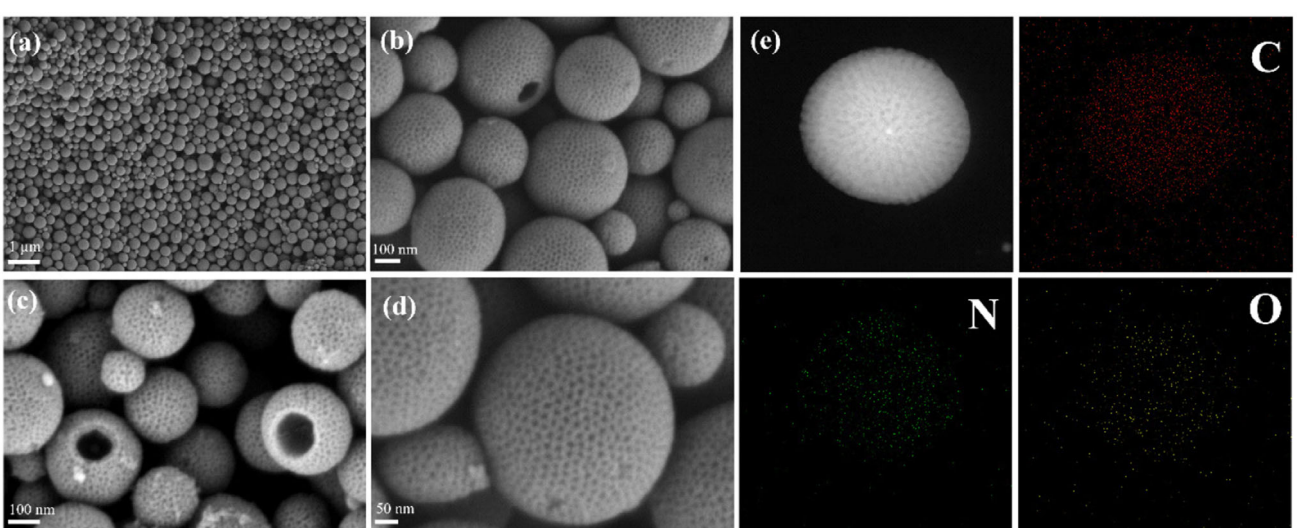
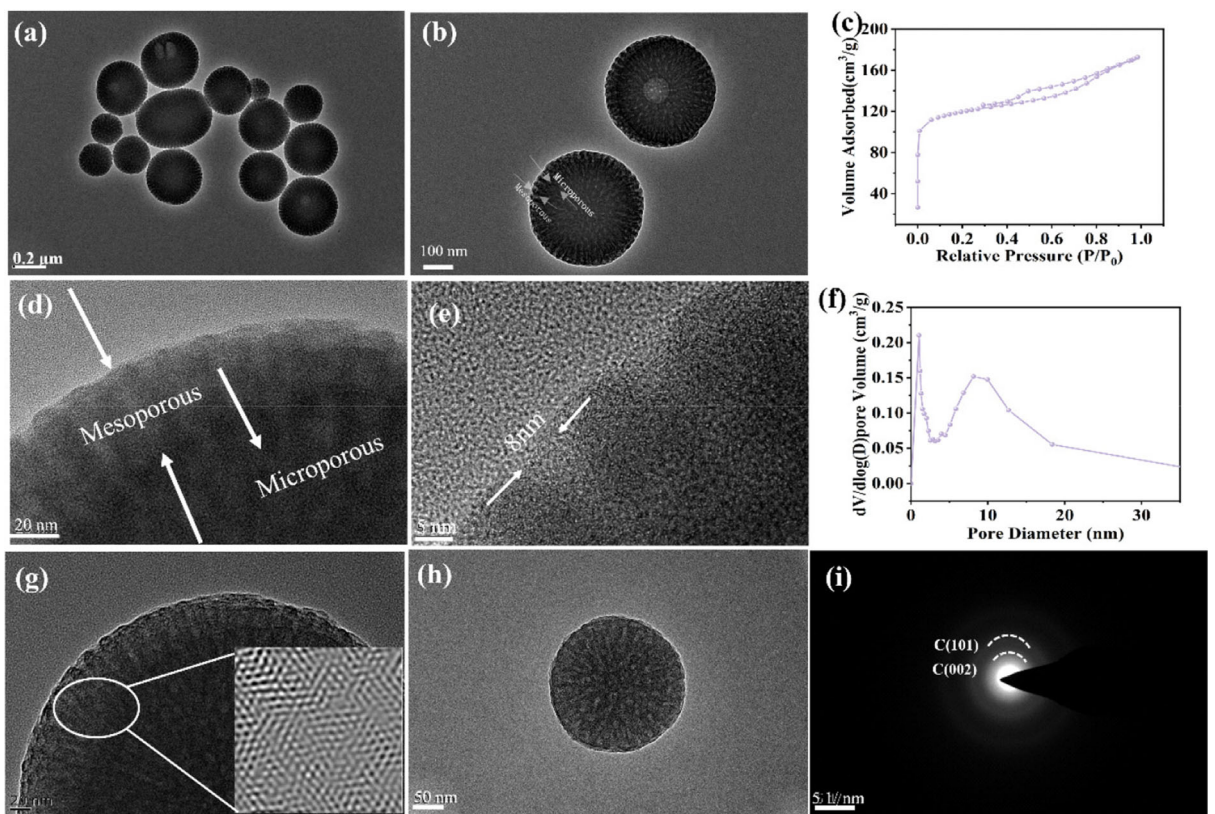


Figure 1. a-d) Scanning electron microscope images of NPCS-40 at different magnifications. e) High-angle annular dark field and energy dispersive X-ray electron spectra of NPCS-40.



**Figure 2.** a–b) Transmission electron microscopy images of NPCs-40 at low magnification. c)  $N_2$  adsorption–desorption isotherm of NPCs-40. d–e) Transmission electron microscopy images of NPCs-40 at high magnification; f) Pore size distribution curve of NPCs-40; g) Fourier transform image of NPCs-40; h,i) Selected area diffraction pattern of NPCs-40.

(101) crystal plane and the typical interlayer spacing of graphite suggests that the material maintains the hexagonal symmetry within the layers, but the interlayer stacking is compressed or has defects. Discrete diffraction spots were not observed, indicating that the sample does not have large single-crystal regions.

The role of the cosolvent in the formation process of porous carbon materials is shown in **Figure 3**. With the increase of ethanol content in the system, the N-doped hierarchical meso-microporous carbon spheres (NPCS)-50 obtained has undergone severe deformation, and the spherical morphology has been

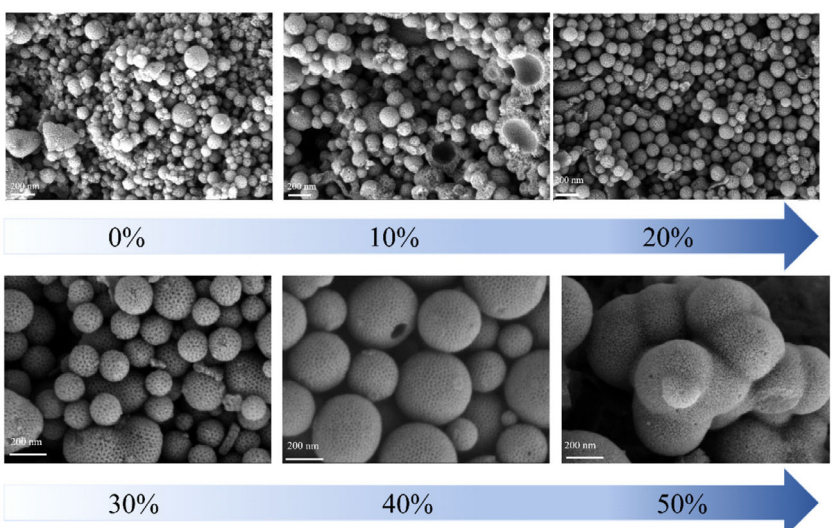


**Figure 3.** Scanning electron microscope images of different ratios of the cosolvent system NPCs-x.

completely changed. The mesoporous structure on the surface of the nanoparticles has disappeared, but microporous structures still exist, indicating that the formation of copolymer micelles has been destroyed. Excessive ethanol (strong polarity) will reduce the hydrophilic-lipophilic balance (HLB) of surfactants, leading to the dissociation of micelle structures, making it impossible for micelles to exist stably, and they cannot act as templates to guide the formation of mesopores, ultimately resulting in the absence of mesoporous structures. Excessive ethanol accelerates solvent evaporation, causing the precursor to shrink rapidly during the drying stage, generating uneven capillary forces, leading to deformation of the nanoparticles.

When the content of ethanol in the ethanol/water research system is too low, the system's polarity is significantly enhanced, making it difficult for the hydrophobic end of surfactants to effectively anchor in the oil phase, resulting in uneven micelle sizes, wider droplet size distribution of microemulsions, coexistence of large and small droplets, and failure of template-guided action. Ethanol, as an assistant surfactant, can reduce interfacial tension and stabilize micelles. However, an excessive amount of water dilutes the ethanol concentration, weakening its regulatory effect and exacerbating micelle coalescence. Excessive water leads to a wider droplet size distribution of microemulsions, losing the uniformity of template size, and ultimately forming a chaotic pore size distribution of mesoporous or nonporous regions. The pore walls soften and fuse, and the mesoporous channels close. The morphology breaks, and nanospheres split into irregular particles or agglomerates. The hollow structure of the mesoporous carbon nanospheres and the micromesoporous double-shell structure can also be observed from the split large-sized nanospheres.

The ethanol/water cosolvent ratio critically determines micelle stability and pore hierarchy. Unlike prior studies using fixed solvent compositions, our method dynamically adjusts the HLB of surfactants, enabling the formation of open mesopores (Figure 3d) without secondary etching. This contrasts with methods requiring harsh post-treatment (e.g., KOH activation or sacrificial templates), which often damage pore structures.

During the synthesis of mesoporous carbon nanospheres, ethylenediamine (EDA) can act as a catalyst to initiate the continuous oxidation of phloroglucinol, and also as a linker to form phloroglucinol-ethylenediamine oligomers in solution through Michael addition or Schiff base reactions. Ethylenediamine decomposes during the carbonization process, releasing nitrogen-containing groups to form nitrogen-doped carbon materials. Nitrogen atoms can adjust the electronic structure of the carbon matrix, enhance surface polarity, and improve the activity of the material in catalysis or energy storage. As shown in Figure S1, Supporting Information, when the content of ethylenediamine is low, the crosslinking is insufficient, the carbon framework is loose, and it is prone to collapse during high-temperature carbonization, resulting in reduced mesopores. Observing the graph of mesoporous carbon nanospheres with a 100  $\mu\text{L}$  ethylenediamine content shows that the surface mesopore size decreases, and some spheres exhibit a microporous surface, indicating the disappearance of the microporous-mesoporous double-shell structure. Moreover, When the ethylenediamine (EDA) content

is low (100  $\mu\text{L}$ ), the crosslinked network is loose (Figure S1a, Supporting Information), resulting in insufficient mechanical strength of the carbon framework, with the specific surface area reduced to  $382 \text{ m}^2 \text{ g}^{-1}$  (Table S1, Supporting Information) and the mesopore volume decreased by 30%. This aligns with the findings of Liu et al.,<sup>[45]</sup> who reported that when the EDA concentration is below 10 wt%, insufficient nitrogen doping (<3 at%) leads to pore wall collapse. At an EDA content of 200  $\mu\text{L}$  (NPCS-40), a balanced mesoporous/microporous double-shell structure is achieved, with the specific surface area increasing to  $428 \text{ m}^2 \text{ g}^{-1}$  (Table 2) and a concentrated pore size distribution (2.275 nm). However, excessive EDA (300  $\mu\text{L}$ ) raises the system pH (>10), destabilizing the F127/P123 micelles, which reduces the mesopore ordering (Figure S1c, Supporting Information), consistent with observations by Xie et al. in similar solvent systems. Observation shows that mesoporous carbon nanoparticles with an ethylenediamine content of 300  $\mu\text{L}$  are blocked by dense crosslinking due to excessive crosslinking, resulting in a decrease in mesoporous content.

Recent studies have confirmed similar concentration-dependent phenomena: Guan et al. found that an EDA content of 20 wt% relative to the resin monomer yielded the optimal pore structure in aqueous systems, while Moussa et al. reported that excessive EDA (>25 wt%) reduced mesoporosity by 40% due to micelle destabilization. In our ethanol/water system (Figure 5), the optimal EDA concentration was lowered to 16.7 wt% (200  $\mu\text{L}$ ), demonstrating the protective effect of the mixed solvent on micelle stability. This advantage can be attributed to: (i) ethanol moderating pH fluctuations during EDA addition, (ii) improved solubility of PPO blocks in the hybrid solvent, and (iii) reduced interfacial tension (as evidenced by the narrower pore size distribution in Figure 2f).

In the system of cosurfactants, in the synthesis system using both P123 and F127 surfactants simultaneously, F127 stabilizes small mesopores ( $\approx 4 \text{ nm}$ ), while P123 directs larger mesopores ( $\approx 8 \text{ nm}$ ), as shown in Figure S2, Supporting Information. When only F127 is used as the surfactant, smaller pore sizes can be observed on the surface of carbon nanospheres, and the trend of pore size increase is more obvious with the increase of P123 content. Under high P123 content, the aperture becomes significantly larger. In the case where only P123 is the surfactant, P123 may cause the aggregation of micelles, leading to the formation of super-large holes with diameters exceeding 15 nm in carbon nanospheres.

As a hydrophobic solvent, TMB can penetrate into the hydrophobic segment (PPO) region of surfactants (such as P123/F127) and increase the volume of the micelle hydrophobic core. The expansion of the volume of the micelle nucleus leads to an increase in the mesoporous pore size formed after carbonization. Observation of Figure S3, Supporting Information, shows that the presence of aperture on the surface of the carbon nanospheres is not observed without the addition of TMB. When the content of TMB is low, the proportion of micropores is large, resulting in pore blocking that reduces accessible  $S_{\text{BET}}$  (e.g., NPCS-0:  $345 \text{ m}^2 \text{ g}^{-1}$  vs. NPCS-40:  $428 \text{ m}^2 \text{ g}^{-1}$ ) and impedes ion diffusion, thus lowering specific capacitance. When the content of TMB is high, the micelle

assembly is disordered, and the mesoporous order decreases, but hierarchical pores (mesoporous + microporous + macroporous) may be accidentally generated.

Phenol formaldehyde resin precursors, as key monomers, significantly affect the pore structure, specific surface area, and uniformity of mesoporous carbon materials through regulating the polymerization reaction kinetics, crosslinking network density, and carbonization behavior, as shown in Figure S4, Supporting Information. When the content of phenol formaldehyde resin is low, the degree of crosslinking is insufficient, the phenol formaldehyde-ethylenediamine network is loose, and the mechanical strength of the carbon framework is low. The mesoporous pore size distribution is wide, the pore walls are thin and prone to collapse, and the proportion of micropores is high. Over-crosslinking hinders the directional assembly of the template.

To analyze the distribution of elements in carbon materials and their surface chemical properties, XPS testing was performed on NPCS-40. As shown in Figure 4, signals can be observed at 284.5, 400, and 532 eV, which correspond to N1s, C1s, and O1s, respectively. As shown in Table 1, the proportions of C, O, and N in NPCS-40 are 87.32%, 5.98%, and 6.69%, respectively. Figure 4b-d shows the element spectra. From the figure, it can be observed that in the C1s spectrum, the peak appearing at 284.8 eV corresponds to C-C, indicating graphitized carbon or  $sp^2$  hybridized carbon, suggesting that the material is mainly

carbon-based. The peak appearing at 285.7 eV corresponds to C-O, originating from surface oxidation or residual oxygen-containing functional groups. A peak appeared at 289.4 eV corresponds to O=C=O (carboxyl) bonds, indicating the presence of oxidation modification on the material surface. O1s shows three distinct peaks at 531.8, 533.2, and 534.6 eV, which correspond to C-O, C=O, and N-O, respectively, indicating that oxygen mainly exists in the form of oxygen-containing functional groups (C=O, C-O), possibly originating from precursor oxidation or surface adsorption. Peaks appearing at 398.5, 401, and 403 eV correspond to pyridine nitrogen, pyrrole nitrogen, and oxidized nitrogen, respectively.

To analyze the crystal structure of the material, we used X-ray diffraction patterns for analysis, as shown in Figure 5a. A characteristic peak appeared near  $23^\circ$ , corresponding to the diffraction of the (002) crystal plane of graphite carbon, indicating the presence of some graphitization structures in the material. Compared to the standard peak position of the (002) crystal plane at  $26^\circ$ , this peak is shifted to a lower angle. The reason for this phenomenon is that nitrogen atoms are larger than carbon atoms, and their embedding in the carbon layer or substitution for carbon atoms will cause lattice expansion. A characteristic diffraction peak with lower intensity appears at  $44.5^\circ$ , representing the (100) crystal plane of the carbon material. With the increase in ethanol content, the peak intensities of both the (002) and (100) crystal planes increase, indicating that in the solvent system with a low concentration of ethanol, the higher the ethanol content in the solvent, the lower the degree of graphitization of the material, and the higher the order. Nitrogen doping leads to interlayer expansion and local order destruction, but does not completely destroy the microcrystalline structure of graphite. The increased interlayer spacing can promote the embedding and desorption of electrolyte ions.

As shown in Figure 5b, to investigate the effect of the cosolvent ratio on the surface defects and structure of carbon materials, Raman spectroscopy tests were conducted. The D peak is usually a defect-induced peak located near  $1350\text{ cm}^{-1}$ , corresponding to defects, edges, or disordered structures in carbon materials. The G peak is usually a graphite peak located near  $1580\text{ cm}^{-1}$ , reflecting the degree of graphitization of carbon materials, i.e., the plane vibration of  $sp^2$  hybridized carbon. The intensity ratio of the D peak to the G peak is used to quantify the defect density of the material. The  $I_D/I_G$  values of NPCS-0, NPCS-10, NPCS-20, NPCS-30, and NPCS-40 are 1.51, 1.44, 1.43, 1.41, and 1.36, respectively, indicating the presence of partially graphitized carbon in the material. The  $I_D/I_G$  indicates that nitrogen atoms are introduced into defects in the form of pyridinic nitrogen, pyrrolic nitrogen, or edge doping, while retaining some graphitized regions. Among them, the ratio of NPS-40 is less than that of other ethanol contents, indicating that a broad and weak 2D peak appears near  $2700\text{ cm}^{-1}$ , indicating that the material contains a small amount of few-layer graphene structures.

Figure 5c,d shows the nitrogen adsorption-desorption isotherms and pore size distribution curves of NPCS-x. According to the observation of Figure 5c, the isotherms are typical type IV isotherms, indicating that the material has a mesoporous

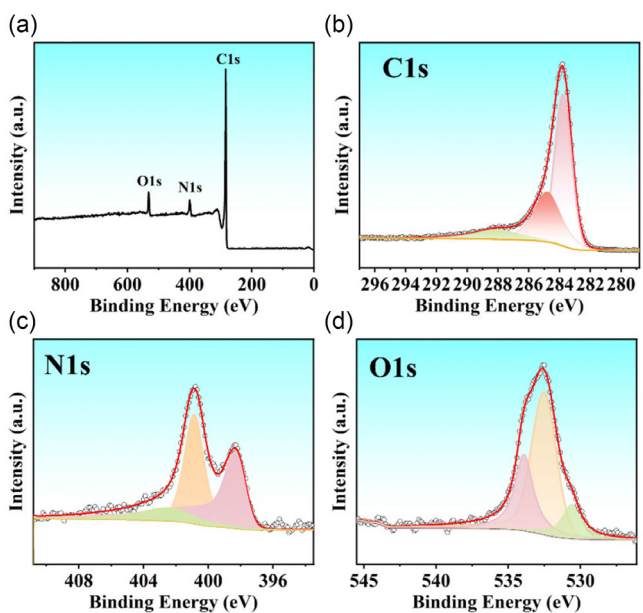


**Figure 4.** a) Total elemental spectrum of NPCS-40. XPS energy spectra of b) C1s; c) N1s; and d) O1s .

**Table 1.** Content of each element in NPCS-40.

NPCS-40	C [%]	O [%]	N [%]
Content	87.32	5.98	6.69

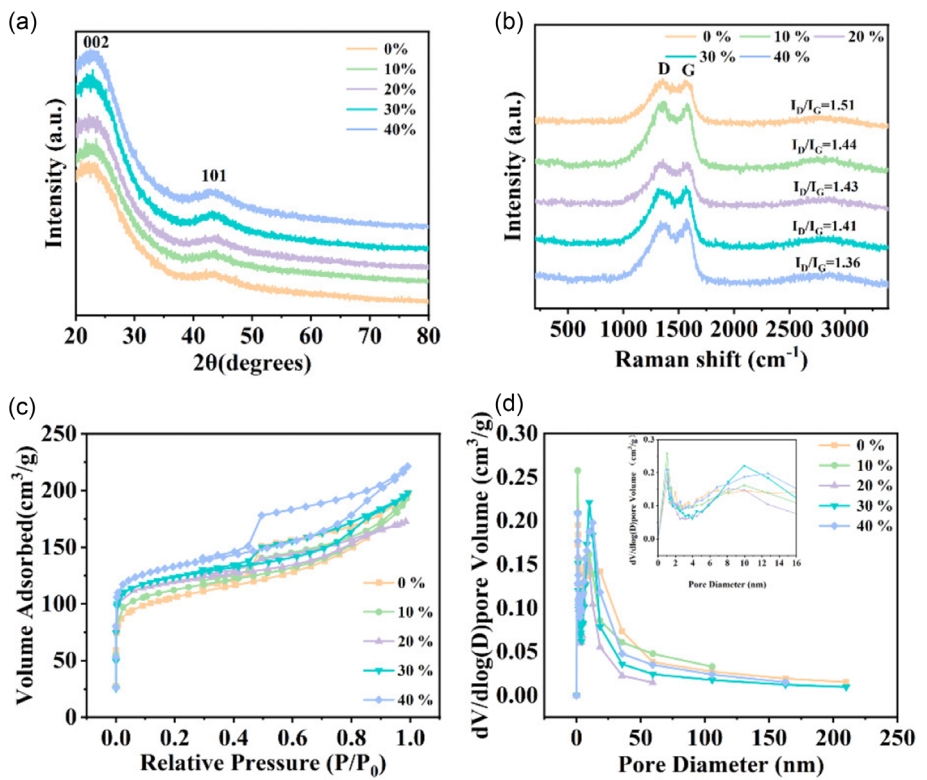


**Figure 5.** a) XRD pattern; b) Raman spectra; c) nitrogen adsorption–desorption curve, and d) pore size distribution of NPCS-x.

structure and is accompanied by a H4-type hysteresis loop, showing that the carbon material has both mesoporous and microporous structures. The adsorption amount increases sharply in the  $P/P_0 = 0.4\text{--}0.8$  range, indicating the capillary condensation phenomenon, corresponding to the filling process of mesopores. Figure 5d shows the pore size distribution of NPCS-x. By observing the pore size distribution, it can be concluded that the materials in the system are all microporous-mesoporous graded porous carbon materials. The micropores and mesopores of NPCS-40 are evenly distributed, corresponding to the TEM observations. **Table 2** lists other pore size parameters of the porous carbon materials in the system, among which NPCS-40 has the highest specific surface area because the pore size distribution of NPCS-40 is the most uniform, and it has the highest mesoporous content among other NPCS-x, with a regular pore size distribution, open and complete channels.

## 2.1. Evaluation of Supercapacitor Performance

### 2.1.1. Three-electrode Test

Figure S5, Supporting Information shows the cyclic voltammetry curves and charge–discharge curves of NPCS-40 prepared with different 1,3,5-trimethylbenzene contents in the microemulsion synthesis system. From the above structural analysis, it can be seen that 2 mL of NPCS-40 has a regular porous structure with uniform micropore-mesopore distribution, and therefore, 2 mL of NPCS-40 has the most excellent electrochemical performance. At low TMB content, while the proportion of micropores increases, the accessible surface area is reduced due to pore blockage and inefficient ion transport pathways, ultimately leading to decreased capacitance, and the cyclic voltammetry (CV) area decreases. At high TMB content, the pore size of the material

**Table 2.** Specific surface area and pore size parameters of NPCS-x.

Samples	$S_{\text{BET}}$ [ $\text{m}^2 \text{ g}^{-1}$ ] <sup>a)</sup>	$V_t$ [ $\text{cm}^3 \text{ g}^{-1}$ ] <sup>b)</sup>	$V_{\text{Mesoporous}}$ [ $\text{cm}^3 \text{ g}^{-1}$ ] <sup>b)</sup>	$V_{\text{Microporous}}$ [ $\text{cm}^3 \text{ g}^{-1}$ ] <sup>b)</sup>	$D_p$ [nm]
NPCS-0	345.49	0.305	0.180	0.125	3.53
NPCS-10	358	0.297	0.175	0.122	3.337
NPCS-20	382.16	0.267	0.158	0.109	2.80
NPCS-30	397.21	0.305	0.185	0.120	3.07
NPCS-40	428.44	0.342	0.210	0.132	2.275
NPCS-50	401.78	0.318	0.165	0.153	2.95

<sup>a)</sup>BET surface area; <sup>b)</sup>Total micropore volume.

increases, the order of mesopores decreases, the pore structure of the material is destroyed, and the ion diffusion is hindered. Therefore, as shown in Figure S5, Supporting Information, 2 mL of NPCS-40 has the largest CV area and the longest discharge time, indicating that 2 mL of NPCS-40 has the largest specific capacitance. Observing Figure S5a, Supporting Information, it can be seen that all samples with different TMB contents have a pseudo-rectangular shape, indicating that all samples have double-layer capacitance behavior, and the hump can be observed, indicating that the electrode material is a capacitance with a mixture of double-layer capacitance and pseudocapacitance. The oxidation-reduction peak of 2 mL is the most significant, and the reason for the pseudocapacitance behavior is the doping of nitrogen elements, with pyridine nitrogen and graphene nitrogen providing redox active sites. The galvanostatic charge-discharge (GCD) curve shown in Figure S5b, Supporting Information, also confirms the analysis of the CV curve. According to Formula (1), the specific capacitance of all samples can be calculated as shown in Table S1, Supporting Information, and 2 ml of NPCS-40 has the largest specific capacitance of  $249 \text{ F g}^{-1}$ . Figure S6a, Supporting Information, shows the electrochemical impedance curves of NPCS-40 with different TMB contents. By observing the curves, it can be seen that the electrochemical impedance of 2 mL of NPCS-40 is the smallest, whether it is the slanting line representing the ion diffusion impedance in the low-frequency region or the radius of the circle representing the material charge transfer resistance in the semicircular region, the impedance of the

2 mL NPCS-40 sample is much lower than that of other TMB content samples, indicating that in the investigation of TMB content, 2 mL is the optimal content.

**Figure 6a,b** shows the cyclic voltammogram and charge-discharge curve of NPCS-x, with ethanol as a cosurfactant, which can reduce the interfacial tension and stabilize the micelles. However, when the water content is too high, it dilutes the concentration of ethanol, making it impossible for the micelles to form stably, resulting in uneven micelle sizes, exacerbating micelle aggregation, and forming a chaotic system with mesoporous, microporous, and nonporous structures coexisting, which affects the electrochemical properties of the material. All curves in Figure 6a are closed pseudo-rectangular curves, which conform to the characteristics of double-layer capacitance. NPCS-40 has a distinct redox peak, indicating the presence of pseudocapacitance in NPCS-40. As the ethanol content decreases, the redox peak gradually decreases until the redox peak in NPCS-0 basically disappears, indicating that the pseudocapacitance gradually decreases. According to the pore size distribution diagram, NPCS-0 has a wider pore size distribution and an uneven structure, causing ion transport to be blocked, and the pseudocapacitance peak is not prominent, and the capacitance is low. According to Figure 6b, the specific capacitance of NPCS-x can be calculated, as shown in **Table 3**. The impedance curve of NPCS-x is shown in Figure S6b, Supporting Information, where NPCS-40 has the smallest ion diffusion resistance and charge transfer resistance, indicating that NPCS-x has the most excellent electrochemical properties.

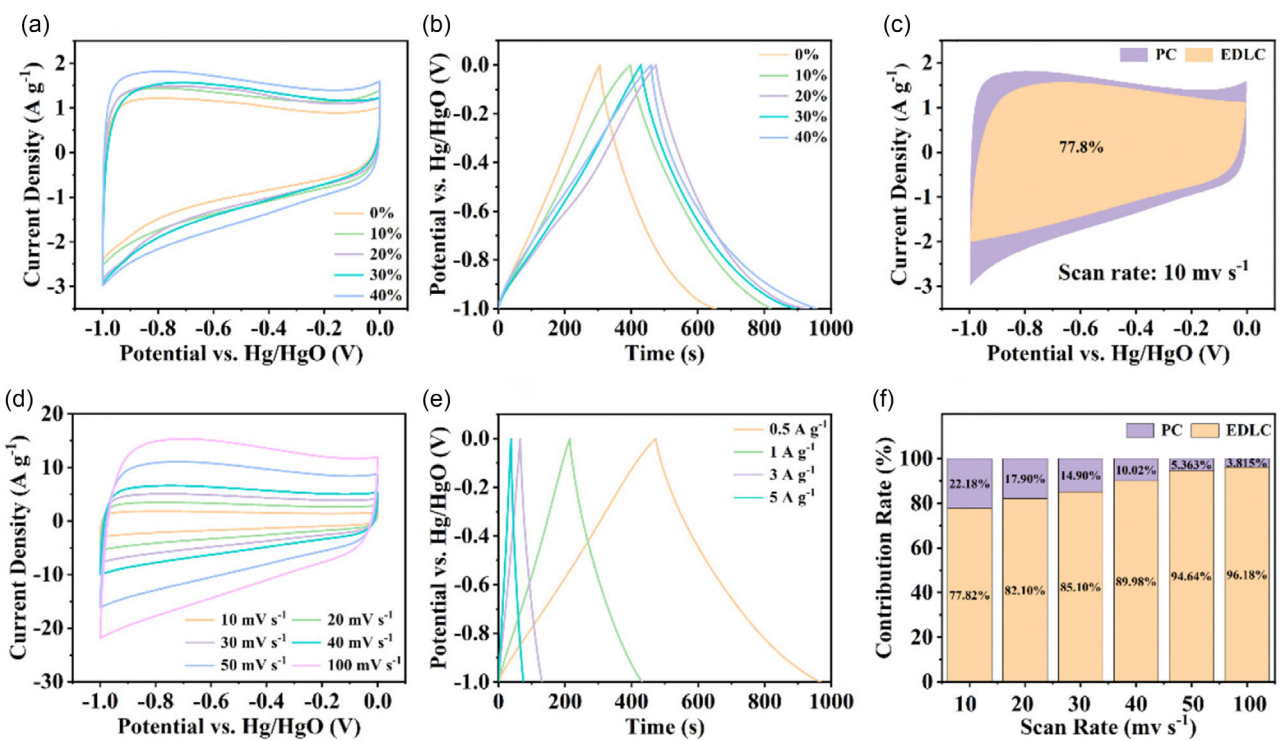


**Figure 6.** a) CV curves at a scan rate of  $10 \text{ mV s}^{-1}$ ; b) GCD curves at a current density of  $0.5 \text{ A g}^{-1}$  of NPCS-x; d) CV curves at different scan rates and e) GCD curves at different current densities of NPCS-40; Contribution plots of NPCS-40 c) bilayer capacitance and f) pseudocapacitance .

**Table 3.** Specific capacitance of NPCS-x at a current density of 0.5 A g<sup>-1</sup>.

Samples	NPCS-0	NPCS-10	NPCS-20	NPCS-30	NPCS-40	NPCS-50
Specific capacitance (F g <sup>-1</sup> )	174.45	229.50	233.00	247.5	249.00	210.30

While NPCS-40 demonstrates optimal performance, the systematic variation in ethanol content reveals distinct structure–property relationships. NPCS-0 exhibits agglomerated particles with a broad pore distribution (Figure 3a), resulting in low capacitance (174.45 F g<sup>-1</sup>) and high impedance (Figure S6b, Supporting Information). Increasing ethanol to 20%–30% (NPCS-20/30) improves micelle uniformity, yielding higher surface areas (382–397 m<sup>2</sup> g<sup>-1</sup>) and capacitances (233–247.5 F g<sup>-1</sup>), but residual pore blockage limits ion kinetics. Conversely, NPCS-50/60 suffer from ethanol-induced micelle dissociation, losing mesoporosity and degrading capacitance by ≈30%. NPCS-40's superiority arises from its balanced micromesoporous double-shell structure, enabling synergistic ion storage (high SSA: 428 m<sup>2</sup> g<sup>-1</sup>) and rapid transport (low R<sub>at</sub>: 0.8 Ω).

The GCD curves of NPCS-40 under different current densities and CV curves under different scan rates were measured, as shown in Figure 6d,e. Figure 6d shows the CV curves of NPCS-40 under different scan rates, where it can be observed that the CV curve is nearly rectangular at a scan rate of 10 mV s<sup>-1</sup>. As the scan rate increases, the rectangular shape gradually decreases, but even when the scan rate increases to 100 mV s<sup>-1</sup>, the CV curve still maintains a pseudo-rectangular shape. Figure 6e shows the GCD curves of NPCS-40 under different current densities, with the curves in isosceles triangle shape indicating the mesoporous carbon material characteristics of NPCS-40.

The analysis of the CV curve shows that this carbon material has a mixed characteristic of double-layer capacitance and pseudocapacitance. Therefore, the capacitance contribution analysis of the CV curve is shown in Figure 6c,f. At a scan rate of 10 mV s<sup>-1</sup>, the contribution ratio of the double-layer capacitance of NPCS-40 is 77.8%. As the scan rate increases, the proportion of double-layer capacitance gradually increases until when the scan rate reaches 100 mV s<sup>-1</sup>, the proportion of double-layer capacitance is 96.18%. This phenomenon is due to the fact that with the increase in scan rate, the slow dynamic process (PC) is affected by the Faraday reaction, leading to instability.

### 2.1.2. Two-electrode Test

Characterizing NPCS-40 with a two-electrode configuration using a symmetrical supercapacitor button cell, with a 6 M KOH solution as the electrolyte, cyclic voltammetry and charge–discharge tests were performed on NPCS-40//NPCS-40 with different TMB contents. The experimental results are shown in Figure S7, Supporting Information. The 2 mL NPCS-40 still exhibits the most excellent electrochemical performance. In the two-electrode test, the CV curve remains pseudo-rectangular and has redox peaks, which verifies the mixed capacitor behavior of the double-layer capacitance and pseudocapacitance of NPCS-40. The near isosceles triangle of the GCD curve indicates the characteristic of the

electrode material being mesoporous carbon material. The specific capacitance of NPC-40 can be calculated to be 75.6, 102 F, 107 F, 118.5 F, and 139.4 F g<sup>-1</sup> based on the charge–discharge curves. Figure S8a, Supporting Information, shows the electrochemical impedance curves of NPCS-40//NPCS-40 with different TMB contents. By observing the curves, it can be seen that the electrochemical impedance of 2 mL of NPCS-40 is still the smallest, corresponding to the three-electrode test results. Whether it is the slanting line representing the ion diffusion impedance in the low-frequency region or the radius of the semicircle representing the material charge transfer resistance, it indicates that in the investigation experiment of symmetrical SCs, the content of 2 mL of NPCS-40 is still the optimal content.

The optimal ratio in the two-electrode test was investigated, and the samples with different solvent ratios were tested. The experimental results are shown in Figure 7a,b. In the CV test and GCD test, NPCS-40 exhibited excellent electrochemical properties, with the largest CV area and discharge time. According to the discharge, the specific capacitance of the material can be calculated as 99.1, 102.8, 102.9, 119.3, and 139.4 F g<sup>-1</sup>. The impedance curves of NPCS-x are shown in Figure S8, Supporting Information, where NPCS-40 has the smallest ionic diffusion resistance and charge transfer resistance, indicating that NPCS-x has the most excellent electrochemical properties.

Figure 7c shows the Ragone plot of power density and energy density for NPCS-40//NPCS-40, as well as a comparison with recently reported SCs. The NPCS-40//NPCS-40 symmetric supercapacitor exhibits an energy density of 7.1 Wh kg<sup>-1</sup> at a power density of 151 W kg<sup>-1</sup>. This value surpasses most recently reported carbon-based SCs (Table 4), including lignin-derived carbon (5.73 Wh kg<sup>-1</sup>), bowl-like carbon (5.08 Wh kg<sup>-1</sup>), and carbon/CNT composites (4.85 Wh kg<sup>-1</sup>). The NPCS-40//NPCS-40 demonstrates excellent high power density and cycling stability in the Ragone plot, with its performance at the upper level of current SCs, as shown in Table 4. Compared with recently reported SCs, its advantages lie in the optimized mesoporous structure and the kinetic improvement brought by the cosolvent, but there is still room for improvement in energy density. In the future, through material composites, electrolyte innovation, and interface regulation, it is expected to achieve dual breakthroughs in energy density and power density, promoting the wide application of SCs in the high-power energy storage field.

Figure 7d-f shows the CV curves and GCD curves of the best-performing sample NPCS-40 under different current densities and scanning rates. NPCS-40 exhibits excellent electrochemical activity at both high and low voltages, indicating its good chemical stability. As the scanning rate increases, the CV curve does not undergo significant distortion. Under different current densities, the material still maintains an isosceles triangle shape, showing excellent rate performance.

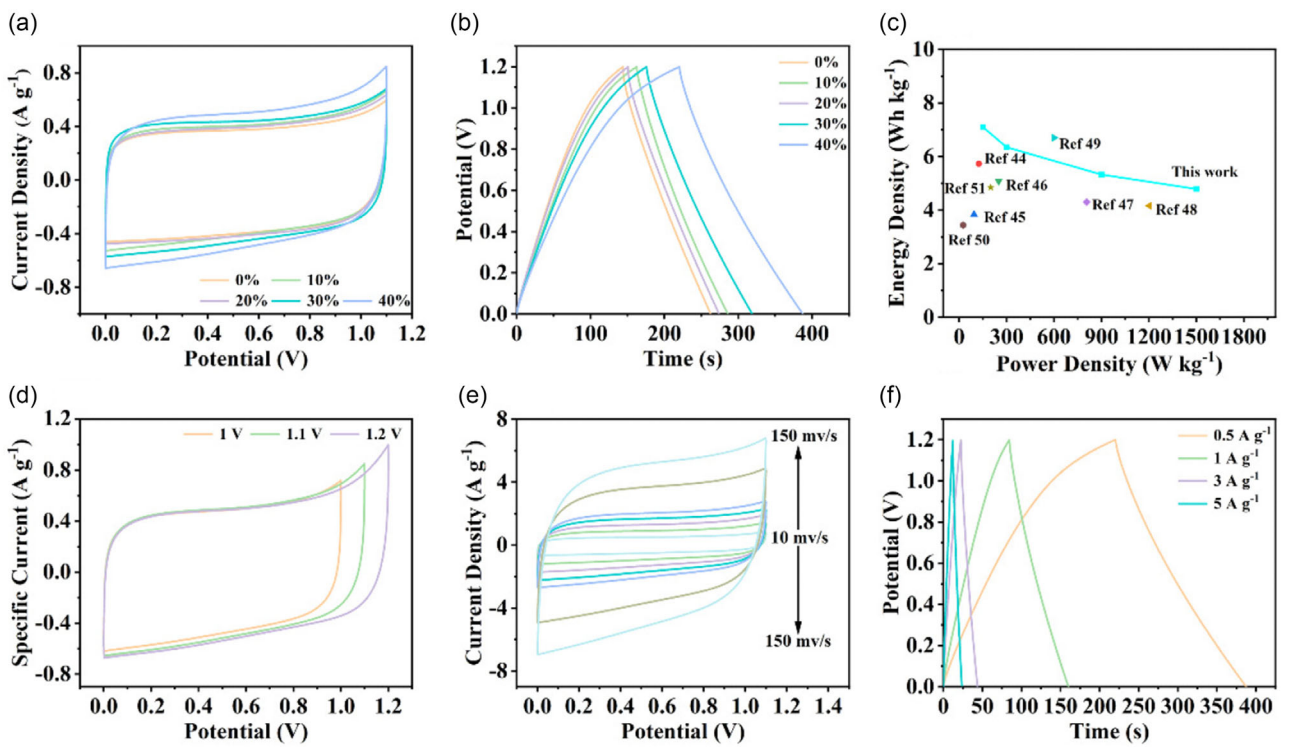


**Figure 7.** a) Cyclic voltammetry and b) charge/discharge curves for NPCS-x//NPCS-x; c) Ragone plots of power density and energy density of NPCS-40//NPCS-40 and comparison of recently reported SCs; d) CV curves of NPCS-40//NPCS-40 at 10 mV/s e) CV curves at different scan rates at 1.1 V potential window. f) GCD curves at different current densities.

Table 4. Electrochemical performances of various SCs reported in recent literature. (The “Ref” column indicates the corresponding reference number in this manuscript’s reference list.)				
No	Electrode materials	Power density [W kg⁻¹]	Energy density [Wh kg⁻¹]	Ref
1	Lignin-based carbon	125	5.73	[47]
2	Reclaimed carbon fiber	93.8	3.84	[48]
3	Bowl-like carbon	250	5.08	[49]
4	Carbon fiber paper	806.5	4.3	[50]
5	CTP-based carbon	1202	4.16	[51]
6	Supercapacitor device with BTO/cellulose	600	6.7	[52]
7	Biomass-derived porous carbon	25	3.44	[53]
8	Carbon/ CNT	199.2	4.85	[54]
9	Multistage structure mesoporous-microporous double shell layer carbon spheres	150	7.1	This work

Figure 8 shows the capacity retention rate change of NPCS-x//NPCS-x after 5000 cycles at a current density of  $2 \text{ A g}^{-1}$ . NPCS-40 is the sample with the highest capacity retention rate at 117%. In the early stages of cycling, the material pores gradually open up, active sites are exposed, the effective reaction area increases, a more stable electrode–electrolyte interface membrane (SEI film) is formed, reducing side reactions, resulting in the material not only not degrading but also showing a “capacity activation” phenomenon. This apparent increase in capacitance during initial cycling stages can be attributed to several synergistic mechanisms: (1) progressive electrolyte penetration into the hierarchical pore structure (microporous core and mesoporous shell) enhances active site accessibility and ion transport kinetics;

(2) redox-active nitrogen functional groups (pyridinic-N and pyrrolic-N, confirmed by XPS in Figure 4) undergo electrochemical activation, contributing additional pseudocapacitance; (3) the unique hollow double-shell architecture (TEM images in Figure 2) minimizes mechanical stress during repeated ion insertion/desertion. Similar “activation” phenomena have been reported for nitrogen-doped carbon materials, where initial cycling improves electrode wettability and pore utilization. The combination of these effects leads to increased effective surface area and stabilized charge storage capacity during prolonged cycling. When the water content is low, the cosolvent forms a uniform microemulsion system during synthesis, promoting the uniform dispersion of the precursor, generating mesoporous structures, and

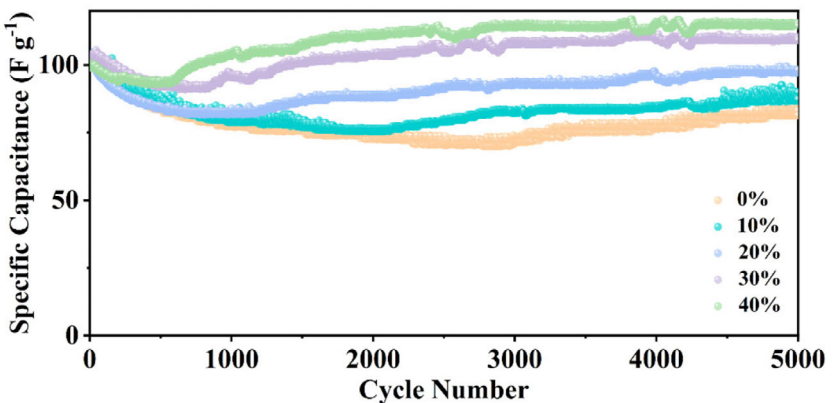


**Figure 8.** Capacity retention rate change of NPCS-x//NPCS-x after 5000 cycles at a current density of  $2 \text{ A g}^{-1}$ .

improving ionic transport efficiency. As the water content increases, the solvent polarity enhances, leading to the instability of surfactant micelles, precursor aggregation, forming nonuniform pores (the proportion of micropores increases), hindering ionic diffusion, and causing the capacity retention rate to gradually decrease.

The Figure S9, Supporting Information, shows the variation curve of the capacity retention rate of NPCS-40/NPCS-40 symmetric SCs with different TMB contents after 5000 charge-discharge cycles at an electric current of  $2 \text{ A g}^{-1}$ . It can be observed from the figure that after 5000 cycles, the capacity retention rate of NPCS-40 is 117%, compared with which, the capacities of other samples have a significant decrease, indicating that NPCS-40 has excellent electrochemical properties.

### 3. Conclusion

This paper adopts a solvent-mediated polymer-induced self-assembly microemulsion to prepare nitrogen-doped mesoporous carbon materials. The size, uniformity, mesopore size, and mesopore ratio of the porous carbon spheres are controlled by adjusting the cosolvent ratio, cosurfactant ratio, oil phase concentration, and monomer concentration. The structure of the porous carbon spheres is analyzed by various analytical methods such as X-ray diffraction (XRD), Brunauer–Emmett–Teller (BET), transmission electron microscope (TEM), HAADF and field-emission scanning electron microscopy (FESEM). The electrochemical performance of NPCS-x is evaluated through cyclic voltammetry, electrochemical impedance spectroscopy (EIS) and charge-discharge tests (GCD). The cosolvent ratio affects the micelle stability, which in turn affects the spherical morphology. When the ethanol content is too low, the nanoparticles deform and form irregular particles and aggregates. When the ethanol content is too high, the mesoporous structure disappears. Under the influence of the structural morphology, the electrochemical properties of the material are affected. When the ethanol content is 40%, the material has the best morphology and performance. The contents of ethylenediamine, surfactant, phloroglucinol, and 1,3,5-trimethylbenzene all have a significant impact on the pore size and openness of the

material. The sample with the optimal ratio has a 1:1 microporous-mesoporous bilayer structure, and the nanoparticles are hollow and open. The hollow open mesoporous-microporous bilayer structure of NPCS-40 has been verified by TEM, BET, and other tests, and this structure also shows excellent performance in electrochemical performance, with the highest specific capacitance, the lowest impedance, and the highest cycling stability. While the current study demonstrates excellent performance in aqueous KOH electrolyte, further investigation of organic (e.g., acetonitrile-based) or ionic liquid electrolytes could expand the operational voltage window and energy density. Similarly, composite formation with pseudocapacitive materials (e.g., metal oxides) may enhance performance but would require careful optimization of interfacial properties. The successful synthesis strategy of solvent-mediated double surfactant polymer-induced microemulsion has successfully synthesized hollow open hierarchical porous carbon nanospheres with a microporous-mesoporous bilayer structure. Nitrogen doping increases the active sites of the carbon material, and the microporous-mesoporous structure increases the ion transport capacity, making the nitrogen-doped mesoporous carbon material show excellent electrochemical performance.

### 4. Experimental Section

#### Reagents and Materials

All chemical reagents were analytically pure. 1,3,5-Trimethylbenzene ( $C_9H_{12}$ ) was purchased from Shanghai Aladdin Biochemical Co. Polyether P123 ( $H(OCH_2CH_2)_x(OCH_2CHCH_3)_y(OCH_2CH_2)_zOH$ ), triblock copolymer Planic F127 ( $M_w = 12,600$ ,  $PEO_{106}PPO_{70}PEO_{106}$ ) were purchased from Sigma-Aldrich Company. Deionized water ( $H_2O$ ) was used for all experiments.

#### Synthesis of Nitrogen-Doped Mesoporous Carbon

Firstly, different ratios of the dual template surfactant Planic F127 and polyether P123 were dissolved in 100 mL of ethanol system with different volume fractions ( $x = V_{\text{EtOH}}/V_{\text{EtOH}} + V_{\text{H}_2\text{O}}$ ,  $x = 0, 10, 20, 30, 40, 50$ , and  $60$ ), and the solution was stirred for 30 min at room temperature to completely dissolve the copolymer. Subsequently, 0.6 g of

resorcinol (phloroglucinol (PG)) was added to the solution and stirring was continued for 30 min, then 2 mL of 1,3,5-trimethylbenzene (TMB) was added with stirring, and a change of the solution from a clarified solution to a milky white solution could be observed after 30 min, and 200  $\mu\text{L}$  of ethylenediamine (EDA) was continued to be added dropwise with stirring, and the reaction mixture was stirred at room temperature at 800 revolutions per minute for 24 h. During the process, the milky-white solution gradually changed to light purple after the addition of ethylenediamine, and the color of the solution gradually became darker with time. 24 h later, the solution became brownish black, and the reaction mixture was centrifuged and dried to obtain the brown powder, which was then preheated at 350 °C under nitrogen atmosphere for 1 h in a tube furnace, then heated at 800 °C for 1 h in a N<sub>2</sub> atmosphere, and the rate of heating was 1 °C min<sup>-1</sup>. NPCS-x ( $x = 0, 10, 20, 30, 40, 50, 60$ ) was obtained.

### Characterization Methods: Electrochemical Analysis

Three-electrode test: Electrochemical characterization was performed using a CHI660E workstation ( $25 \pm 1$  °C) with a three-electrode configuration. The working electrode was fabricated through sequential processing: (1) homogenizing active material/acetylene black/PTFE (8:1:1 w/w) in agate mortar, (2) incorporating PTFE binder solution (5 wt%) dropwise, (3) coating slurry onto 1 cm<sup>2</sup> nickel foam substrate, (4) vacuum drying at 75 °C for 12 h, followed by calendaring. Cyclic voltammetry ( $-1.0$ – $0$  V v.s. Hg/HgO), galvanostatic charge–discharge, and EIS measurements were conducted in 6 M KOH electrolyte with a platinum counter electrode. Specific capacitance was calculated via

$$Cs = I\Delta t / (m\Delta V) \quad (1)$$

$I$  is the constant current,  $\Delta t_c$  is the charge time,  $\Delta t_d$  is the discharge time,  $m$  is the weight of the active material on the electrode, and  $\Delta V$  is the voltage window.

Two electrodes: The energy storage device was assembled in a CR2032 coin-type configuration through standardized electrode fabrication protocols. Ternary composite electrodes were prepared by homogeneously mixing electroactive components with conductive additives and polymeric binders at an 80:10:10 mass ratio. This viscous ink was precisely deposited onto circular nickel foam current collectors ( $\varnothing 10$  mm) using the doctor-blade deposition technique, followed by sequential processing steps: (1) solvent evaporation under a temperature-controlled vacuum environment (70 °C/12h), (2) mechanical densification via uniaxial compression (10 MPa) to enhance interfacial contact. Cell assembly: matched electrode pairs (mass variation <5%) were separated by a polypropylene membrane, immersed in 6 M KOH electrolyte, and stacked in electrode/separators/electrode configuration.

Electrochemical characterization: CV ( $-1.0$ – $0$  V), GCD (1–5 A g<sup>-1</sup>), and EIS (100 kHz–10 mHz) were performed using a CHI660E workstation.

Performance metrics: specific capacitance calculated from GCD data, with cycle stability assessed through 10 000 charge–discharge cycles. Using the following formulas, cycle life tests on a blue battery tester were used to determine the electrode materials' specific capacitance (F g<sup>-1</sup>), energy density (E, Wh kg<sup>-1</sup>), and power density (P, W kg<sup>-1</sup>)

$$Cs = 2I(A)\Delta t(s) / (m_s(g)\Delta V(V)) \quad (2)$$

where  $I$  (A) is the constant current,  $\Delta t$  (s) is the discharge time,  $m_s$  (g) is the quality of active material on the individual electrodes, and  $\Delta V$  (V) is the voltage window after subtracting the IR fall time.

$$E = (Cs \times V^2) / (2 \times 4 \times 3.6) \quad (3)$$

$$P = (E \times 3600) / \Delta t \quad (4)$$

where the symbols for mass-based energy density, average power density, and discharge duration are, respectively,  $E$  (Wh kg<sup>-1</sup>),  $P$  (W kg<sup>-1</sup>), and  $\Delta t$  (s).

### Supporting Information

The online version contains supplementary material, including: Revised EIS spectra with clear semicircle/Warburg regions (Figs. S6, S8). CV/GCD curves for all parameter variations (Figs. S1–S5, S7). Post-cycling morphology analysis (Fig. S10: TEM pore evolution, Fig. S11: SEM surface changes). Full BET parameter tables (Tabs S2–S3: XPS peak fitting details (Fig. S12).

### Acknowledgements

This research was supported by the Research Program of Application Foundation of Qinghai Province (No. 2024-ZJ-787).

### Conflict of Interest

The authors declare no conflict of interest.

### Author Contributions

**Zhi-Yan Bai:** data curation (lead), formal analysis (lead); software (lead), supervision (lead); writing—original draft (lead); **Zha-Xi Wan-Me:** formal analysis (supporting); software (supporting); **Ji Cai-Rang:** formal analysis (supporting); software (supporting); **Peng Liu:** formal analysis (supporting); software (supporting); **Fu Yang:** formal analysis (supporting); software (supporting); **Yu-Long Xie:** conceptualization, funding acquisition, investigation, project administration, supervision, writing—review & editing.

### Data Availability Statement

The data that support the findings of this study are available in the supplementary material of this article.

**Keywords:** dual-template self-assembly • energy storage • hierarchical porous carbon • nitrogen doping • supercapacitors

- [1] Y. Liu, M. Xiao, S. Liu, X. Zhao, Y. Tian, X. Wang, *Carbon* **2022**, *200*, 361.
- [2] R. Lin, G. Li, Q. He, J. Song, Y. Ma, Y. Zhan, M. Yuan, Q. Li, D. Chao, X. Li, et al., *J. Am. Chem. Soc.* **2024**, *146*, 26983.
- [3] A. Siyasukh, Y. Chimupala, N. Tonanon, *Carbon* **2018**, *134*, 207.
- [4] S. Luan, W. Li, X. Hou, Z. Guo, W. Li, Y. Song, X. Zhang, Q. Wang, *Carbon* **2019**, *151*, 18.
- [5] Y. Mo, J. Du, H. Lv, Y. Zhang, A. Chen, *Diamond Relat. Mater.* **2021**, *111*, 108206.
- [6] B. You, F. Kang, P. Yin, Q. Zhang, *Carbon* **2016**, *103*, 9.
- [7] K. Xu, W. Li, Q. Liu, B. Li, X. Liu, L. An, Z. Chen, R. Zou, J. H. Hu, *J. Mater. Chem. A* **2014**, *2*, 4795.
- [8] T. Chen, L. Dai, *J. Mater. Chem. A* **2014**, *2*, 10756.
- [9] Yu. M. Volkovich, *Russ. J. Electrochim.* **2021**, *57*, 311.

- [10] M. Ferreira, S. Güney, I. Kuźniarska-Biernacka, O. S. G. P. Soares, J. L. Figueiredo, M. F. R. Pereira, I. C. Neves, A. M. Fonseca, P. Parpot, *New J. Chem.* **2021**, *45*, 12622.
- [11] Y. Zheng, K. Chen, K. Jiang, F. Zhang, G. Zhu, H. Xu, *J. Energy Storage* **2022**, *56*, 105995.
- [12] L. Yao, Q. Wu, Z. Zhang, J. Zhang, D. Wang, Y. Li, X. Ren, H. Mi, L. Deng, Z. Zheng, *Adv. Mater.* **2018**, *30*, 1706054.
- [13] Y. Yan, G. Chen, P. She, G. Zhong, W. Yan, B. Y. Guan, Y. Yamauchi, *Adv. Mater.* **2020**, *32*, 2004654.
- [14] X. Gao, P. Wang, Z. Pan, J. P. Claverie, J. Wang, *ChemSusChem* **2020**, *13*, 1226.
- [15] Y. Ji, J. Du, A. Chen, X. Gao, M. Peng, *ChemSusChem* **2025**, *18*, e202401557.
- [16] Y. Zhou, H. Qi, J. Yang, Z. Bo, F. Huang, M. S. Islam, X. Lu, L. Dai, R. Amal, C. H. Wang, et al., *Energy Environ. Sci.*, **2021**, *14*, 1854.
- [17] C. Wang, *Adv. Powder Mater.* **2022**, *1*, 100018.
- [18] S. Yuan, Q. Gao, C. Ke, T. Zuo, J. Hou, Zhang J., *ChemElectroChem* **2021**, *9*, e202101182.
- [19] R. Ragavan, *Microporous Mesoporous Mater.* **2022**, *338*, 111959.
- [20] S. Reenu, L. Phor, A. Kumar, S. Chahal, *J. Energy Storage* **2024**, *84*, 110698.
- [21] F. Wang, Y. Liu, M. Peng, M. Yang, Y. Chen, J. Du, A. Chen, *ACS Catal.* **2024**, *14*, 16434.
- [22] Z. Liu, W. Li, W. Sheng, S. Liu, R. Li, C. Huang, Y. Xiong, L. Han, W. Zhen, Y. Li, et al., *Small* **2024**, *20*, 2403777.
- [23] V. M. Ortiz-Martínez, L. Gómez-Coma, A. Ortiz, I. Ortiz, *Rev. Chem. Eng.* **2020**, *36*, 771.
- [24] M. Gradielski, M. Duvail, P. M. De Molina, M. Simon, Y. Talmon, T. Zemb, *Chem. Rev.* **2021**, *121*, 5671.
- [25] A. Serrà, E. Vallés, *Catalysts* **2018**, *8*, 395.
- [26] F. Chu, X. Li, W. Yuan, H. Zhu, Y. Qin, S. Zhang, N. Yuan, B. Lin, J. Ding, *Funct. Mater. Lett.* **2018**, *11*, 1850015.
- [27] A. Daraghmeh, S. Hussain, A. U. Haq, I. Saadeddin, L. Servera, J. M. Ruiz, *J. Energy Storage* **2020**, *32*, 101798.
- [28] W. Xin, Y. Song, *RSC Adv.* **2015**, *5*, 83239.
- [29] M. Chen, L.-L. Shao, X.-W. Lv, G.-C. Wang, W.-Q. Yang, Z.-Y. Yuan, X. Qian, Y.-Y. Han, A.-X. Ding, *Chem. Eng. J.* **2020**, *390*, 124633.
- [30] J. Yan, C. Guo, X. Guo, X. H. Tong, *J. Electron. Mater.* **2022**, *51*, 1021.
- [31] Y. Ji, W. Xu, A. Chen, J. Du, S. Hou, *Mater. Today Energy* **2025**, *47*, 101746.
- [32] C. Liu, J. Wang, J. Li, X. Hu, P. Lin, J. Shen, X. Sun, W. Han, L. Wang, *J. Mater. Chem. A* **2016**, *4*, 11916.
- [33] K. Li, J. Li, M. Lu, H. Li, X. Wang, *Desalin. Water Treat.* **2016**, *57*, 24004.
- [34] Z. Liu, W. Li, W. Sheng, S. Liu, R. Li, Q. Li, D. Li, S. Yu, M. Li, Y. Li, et al., *J. Am. Chem. Soc.* **2023**, *145*, 5310.
- [35] Y.-L. Xie, Q.-N. Guo, *J. Solid State Electrochem.* **2022**, *26*, 1013.
- [36] O. S. Djandja, L. Yin, Z. Wang, P.-G. Duan, D. Xu, K. Kapusta, *J. Energy Storage* **2023**, *60*, 106588.
- [37] G. Moussa, S. Hajjar-Garreau, P.-L. Taberna, P. Simon, C. E.-F. Matei Ghimeau, *J. Carbon Res.* **2018**, *4*, 20.
- [38] L. Peng, H. Peng, W. Li, D. Zhao, *Nat. Protoc.* **2023**, *18*, 1155.
- [39] P. Forouzandeh, V. Kumaravel, S. C. Pillai, *Catalysts* **2020**, *10*, 969.
- [40] A. González, E. Goikolea, J. A. Barrena, R. Mysyk, *Renewable Sustainable Energy Rev.* **2016**, *58*, 1189.
- [41] D. J. Pandya, P. Muthu Pandian, I. Kumar, A. Parmar, S. Sravanthi, N. Abd Al-saheb, A. J. Arun, V. Supercapacitors, *Mater. Today: Proc.* **2023**, *139*, 72.
- [42] B. Y. Guan, L. Yu, X. Wen, *J. Am. Chem. Soc.* **2022**, *144*, 134.
- [43] J. Du, Q. Han, Y. Chen, M. Peng, L. Xie, *Angew. Chem.* **2024**, *63*, e202411066.
- [44] F. Wei, *Chem. Eng. J.* **2022**, *450*, 137919.
- [45] C. Liu, J. Wang, J. Li, M. Zeng, R. Luo, J. Shen, X. Sun, W. Han, L. Wang, *ACS Appl. Mater. Interfaces* **2016**, *8*, 7194..
- [46] R. Ragavan, et al., *Inorg. Chem. Commun.* **2024**, *162*, 112257.
- [47] S. Zhai, K. Li, C. Li, C. Zhai, Q. Han, Z. Zhang, Y. Fu, X. Li, K. Jin, Z. Cai, T. Zhao, *J. Energy Storage* **2024**, *85*, 111036.
- [48] C. Zhao, J. Guo, J. Fan, X. Zhang, C. Zhao, S. S. Chen, *J. Energy Storage* **2022**, *46*, 103786.
- [49] M. Lu, Y. Zhao, Q. Tang, H. Ren, H. Wang, L. Wang, *Colloids Surf., A* **2023**, *665*, 131243.
- [50] J. Chen, J. Xie, C. Q. Jia, C. Song, J. Hu, H. E. Li, *Chem. Eng. J.* **2022**, *450*, 137938.
- [51] B. Mo, L. Wang, L. Li, B. Han, G. Xu, K. Wang, J. Zhang, Z. Ni, X. He, W. S. Zhou, *J. Chem. Eng. Jpn.* **2023**, *56*, 2217863.
- [52] R. Martínez, E. Cruz, S. Zografos, J. Soto, R. Palai, C. R. Cabrera, *J. Energy Storage* **2024**, *81*, 110527.
- [53] Y. Zhang, Y. Cai, T. Li, M. Wang, X. Chen, Y. Xu, *J. Mater. Sci.: Mater. Electron.* **2024**, *35*, 116.
- [54] D. Thillaikkaras, S. Karthikeyan, R. Ramesh, P. Sengodan, D. Kavitha, M. Muthubalasubramanian, *Carbon Lett.* **2022**, *32*, 1481.

Manuscript received: May 29, 2025

Revised manuscript received: August 24, 2025

Version of record online: